Supplement of Earth Syst. Sci. Data, 15, 2295–2327, 2023
https://doi.org/10.5194/essd-15-2295-2023-supplement

Supplement of

Indicators of Global Climate Change 2022: annual update of large-scale indicators of the state of the climate system and human influence

Piers M. Forster et al.

Correspondence to: Piers M. Forster (p.m.forster@leeds.ac.uk)

Section numbers match the main paper.

S3. Greenhouse gas concentrations

Naming conventions and details for Sect. 3 of the main paper and here follow AR6 WGI Chapter 2 (Gulev et al., 2021).

Table S1: Annual mean concentrations of well-mixed greenhouse gases (GHGs) in 2022, 2019, 1850 and 1750. Except for CO_2, CH_4 and N_2O, concentrations all are in parts per trillion [ppt]. For halogenated gases, concentrations are stated for each gas, with equivalents for HFCs, PFCs and Montreal gases given as the radiative equivalent of the most abundant gas in each category.

Greenhouse gas	1750	1850	2019	2022
CO_2 [ppm]	278.3	285.5	410.1	417.1
CH_4 [ppb]	729.2	807.6	1866.3	1911.9
N_2O [ppb]	270.1	272.1	332.1	335.9
NF_3	0	0	2.1	2.7
SF_6	0	0	9.9	11
SO_2F_2	0	0	2.5	2.8
HFCs as HFC-134a-eq	0	0	237.7	287.2
HFC-23	0	0	32.5	36.1
HFC-32	0	0	20.4	31.1
HFC-125	0	0	29.5	39.7
HFC-134a	0	0	107.6	124.5
HFC-143a	0	0	24	28.9
HFC-152a	0	0	7.2	7.5
HFC-227ea	0	0	1.6	2.1
HFC-236fa	0	0	0.2	0.2
HFC-245fa	0	0	3.1	3.7
HFC-365mfc	0	0	1.1	1.2
HFC-43-10mee	0	0	0.3	0.3
PFCs as CF_4-eq	34	34	109.4	114.2
CF_4	34	34	85.6	88.4
C_2F_6	0	0	4.8	5.1
C_3F_8	0	0	0.7	0.7
c-C_4F_8	0	0	1.8	1.9
n-C_4F_{10}	0	0	0.2	0.2
n-C_5F_{12}	0	0	0.1	0.2

n-C_6F_{14}	0	0	0.2	0.2
i-C_6F_{14}	0	0	0.1	0.1
C_7F_{16}	0	0	0.1	0.1
C_8F_{18}	0	0	0.1	0.1
Montreal gases as CFC-12-eq	8.5	8.5	1031.8	1016.6
CFC-11	0	0	226.2	219.6
CFC-12	0	0	502.9	493.3
CFC-112	0	0	0.4	0.4
CFC-112a	0	0	0.1	0.1
CFC-13	0	0	3.3	3.4
CFC-113	0	0	69.8	68.2
CFC-113a	0	0	0.9	1
CFC-114	0	0	16.3	16.3
CFC-114a	0	0	1	1
CFC-115	0	0	8.7	8.8
HCFC-22	0	0	246.8	251.8
HCFC-31	0	0	0.1	0.1
HCFC-124	0	0	1	0.9
HCFC-133a	0	0	0.4	0.5
HCFC-141b	0	0	24.4	24.6
HCFC-142b	0	0	22.2	21.9
CH_3CCl_3	0	0	1.6	0.9
CCl_4	0	0	78.1	74
CH_3Cl	457	457	540.8	538
CH_3Br	5.3	5.3	6.5	6.4
CH_2Cl_2	6.9	6.9	36.8	40.7
$CHCl_3$	4.8	4.8	8.8	8.7
Halon-1211	0	0	3.3	3
Halon-1301	0	0	3.3	3.4
Halon-2402	0	0	0.4	0.4

S4. Effective radiative forcing (ERF)

S4.1 Well-mixed greenhouse gas ERF methods

Radiative forcings (RFs)from CO_2, CH_4 and N_2O use the simplified formulas from concentrations in Meinshausen et al. (2020), derived from an updated functional fit to the line-by-line radiative transfer results by Etminan et al. (2016). These formulas are, to first order, logarithmic with CO_2 concentrations, and a square-root dependence for CH_4 and N_2O, with additional corrections and radiative band, overlaps between gases. RF is converted to ERF using scaling factors (1.05, 0.86 and 1.07 for CO_2, CH_4 and N_2O respectively) that account for tropospheric and land-surface rapid adjustments (Smith et al., 2018a; Hodnebrog et al., 2020a). ERF from other GHGs is assumed to scale linearly with their concentration based on their radiative efficiencies, expressed in W m^{-2} ppb^{-1} (Hodnebrog et al., 2020b, Smith et al., 2021b). A scaling factor translating RF to ERF is implemented for CFC-11 (1.13) and CFC-12 (1.12) (Hodnebrog et al., 2020a), whereas no model evidence exists to treat ERF differently to RF for other halogenated gases.

Relative uncertainties in the ERF for CO_2 (± 12%), CH_4 (± 20%) and N_2O (± 14%) are unchanged from AR6. These stem from a combination of spectroscopic uncertainties and uncertainties in the adjustment terms converting RF to ERF; uncertainties in the volume mixing concentrations themselves are assessed to be small (Sect. 2.2). Uncertainties in the ERF from halogenated gases are treated individually and are assessed as ±19% for gases with a lifetime of 5 or more years and ±26% for shorter-lifetime gases. In AR6, a ±19% uncertainty was applied to the sum of the ERF from all halogenated gases. To maintain a consistent uncertainty range across the sum of ERF from halogenated gases with AR6, we inflate the uncertainty in each individual gas by a factor of 2.05. Uncertainties are applied by scaling the full ERF time series for each gas.

S4.2 Aerosol ERF methods

Aerosol ERF is a combination of contributions from aerosol-radiation interactions (ERFari) and aerosol-cloud interactions (ERFaci).

S4.2.1 Aerosol-radiation interactions

Contributions to ERFari are assumed to scale linearly with certain SLCF emissions in Sect. 2.3 (SO_2, BC, OC, NH_3, NOx and VOC) or concentrations (CH_4, N_2O and ozone-depleting halocarbons) of primary aerosols and chemically active precursor species. The coefficients converting emissions or concentrations of each SLCF into ERF and its uncertainty come from Chapter 6 of AR6 WGI (Szopa et al., 2021), originally from CMIP6 AerChemMIP models (Thornhill et al., 2021a). We scale these coefficients to reproduce the headline AR6 WGI ERFari assessment of -0.3 W m^{-2} from 1750 to 2005-2014. Uncertainties are applied as a scale factor for each species and applied to the whole time series.

The inclusion of more species that affect ERFari differs from the AR6 WGI calculation of ERFari in Chapter 7, which only used SO_2, BC, OC and NH_3 (Smith et al., 2021b). In the update, these four species remain the dominant aerosol and aerosol precursors. Additionally, these coefficients have changed slightly due to switching to CMIP6 era data. In AR6, the coefficients' scaling emissions to ERF for SO_2, BC, OC and NH_3 were provided by CMIP5-era models (Myhre et al., 2013a). The additional coefficients and slight changes to their magnitude had an imperceptible effect on the results but have been included to align with current best practice. This might be important in future years as NOx and VOC precursors might make up a larger fraction of ERFari.

S4.2.2 Aerosol-cloud interactions

ERFaci is estimated by assuming a logarithmic relationship with the change in cloud droplet number concentration (CDNC) as

$$\mathrm{ERFaci} = \beta \log (1 + \Delta \mathrm{CDNC}) \qquad \text{(S1)}$$

$$\Delta \mathrm{CDNC} = s_{\mathrm{SO2}} \Delta E_{\mathrm{SO2}} + s_{\mathrm{BC}} \Delta E_{\mathrm{BC}} + s_{\mathrm{OC}} \Delta E_{\mathrm{OC}}, \qquad \text{(S2)}$$

where s_{SO2}, s_{BC} and s_{OC} are sensitivities of the change in CDNC with the change in emissions of SO_2, BC and OC respectively (ΔE). This relationship is fit to estimates of ERFaci in 13 CMIP6 models contributing results to the piClim-histaer and histSST-piAer experiments of RFMIP and AerChemMIP, respectively, to CMIP6. The ERFaci in these 13 models is estimated using the approximate partial radiative perturbation (APRP) method (Taylor et al., 2007; Zelinka et al., 2014).

The s_{SO2}, s_{BC} and s_{OC} values from each model are combined into a kernel density estimate and sampled 100,000 times to provide a CMIP6-informed distribution of these parameters. To obtain β for each sample given (s_{SO2}, s_{BC}, s_{OC}), a target ERFaci value for 1750 to 2005-2014 is drawn from the headline AR6 distribution of -1.0 [-1.7 to -0.3] W m^{-2} and eq. (S1) rearranged. This follows a very similar procedure to AR6 and is based on Smith et al. (2021a) with three updates. Firstly, the relationships in eqs. (S1) and (S2) are slightly updated and simplified. Secondly, an additional two CMIP6 models have become available since the AR6 WG1 assessment, which expands the sampling pool for coefficients from 11 to 13. Thirdly, a slight error in computing ERFaci from APRP from the CMIP6 models in Smith et al. (2021a) has been corrected (Zelinka et al., 2023).

Estimates of aerosol ERF do not include explicit changes from the introduction of the International Maritime Organization (IMO) convention on sulfur content in fuel, though some of the impact of the legislation is implicitly captured by our activity-data proxy estimate of emissions (Sect. 2.3). This may have reduced SO_2 emissions from the shipping sector even more than we estimate from the impacts of COVID-19 alone. A secondary effect of shipping that we do not include is its spatial pattern. Unlike the majority of anthropogenic emissions which are land-based, shipping emits primarily in oceanic regions. Ship tracks very readily form in oceanic shallow stratocumulus regions (Watson-Parris et al., 2022), and the reduction of sulfate aerosol (an efficient cloud condensation nuclei) may reduce the magnitude (increase the positivity) of ERFaci more so than an equivalent reduction in emissions from another sector. One estimate puts this effect at up to +0.27 W m^{-2} (Yuan et al. 2022). The evidence for a different efficacy of ship-track SO_2 emissions compared to land-based SO_2 emissions will be reviewed in future should further research emerge.

S4.3 Ozone ERF methods

Ozone ERF is derived from CMIP6 model-based estimates. As in AR6 WGI Chapter 7, we use results from Earth system models (ESMs) and chemical transport models that produced historical ozone RF estimates in Skeie et al. (2020). We use only the six ESMs in Skeie et al. (2020) that are independent, include stratospheric and tropospheric ozone chemistry, and produce observationally plausible distributions of present-day ozone (Smith et al., 2021b). From these model time series of ozone RF from 1850 to 2014, we infer the sensitivity of ozone RF to emissions of NOx, VOC and CO; concentrations of CH_4, N_2O and ozone-depleting halogens; and global mean surface temperature (GMST) anomaly. The fit of the precursor sensitivities and GMST is performed using a least-squares curve fit, with the search bounds of each coefficient set to the 90% range (1.645 times standard deviation) of each species' contribution to ozone forcing determined using single-forcing experiments in Thornhill et al. (2021a) from a number of CMIP6 models contributing to AerChemMIP. UKESM1-0-LL has an anomalously large stratospheric ozone depletion response to halocarbons (Keeble et al., 2021), so this model was excluded when constructing these ranges. In CMIP6, experimental results that vary CO and VOC emissions separately are not available, so individual contributions from CO and VOC to the CO+VOC total are based on their fractional contributions from ACCMIP (CMIP5-era) models in Stevenson et al. (2013). For the global mean temperature contribution, we use the model responses to ozone forcing per degree warming in chemistry-enabled models in abrupt-4xCO2 experiments (Thornhill et al., 2021b). Following AR6, we do not differentiate between stratospheric and tropospheric ozone, and we also assume that ERF is the same as RF as there is limited model evidence to suggest otherwise.

S4.4 ERF from other anthropogenic forcers

Minor categories of anthropogenic forcers include contributions from land use and land-use change other than via GHG emissions, aviation contrails and contrail-induced cirrus; stratospheric water vapour from methane oxidation; and light absorbing particles on snow and ice.

The methodology to estimate ERF from land use and land-use change has been updated to use a scale factor with cumulative CO_2-LUC emissions since 1750. This provides a similar time history to the land use ERF in AR6 and links this directly to land use ERF in future scenarios (Smith et al., 2021b). We anchor the 1750-2019 assessment to be the same as AR6 at -0.20 [-0.30 to -0.10] W m^{-2} under this updated methodology. With this, albedo changes and effects of irrigation (mainly via low-cloud amount) are accounted for, while other biogeophysical effects of land use and land-use change are deemed to be of second-order importance (Smith et al., 2021b).

Stratospheric water vapour from methane oxidation was assessed to be 0.05 [0.00 to 0.10] W m^{-2} in AR6 for 1750-2019. We use the same scale factor applied to methane ERF used in AR6.

The ERF from light absorbing particles on snow and ice (LAPSI) is assumed to scale with emissions of black carbon. As in AR6, the contribution from brown carbon is assumed to be negligible. We align the coefficient that converts BC emissions to ERF from LAPSI to be 0.08 [0.00 to 0.18] W m^{-2} for 1750-2019.

To estimate ERF from aviation contrails and contrail-induced cirrus in AR6, emissions of NOx from the aviation sector in CEDS were scaled to reproduce an ERF of 0.0574 [0.019 to 0.098] W m^{-2} for 1750-2018 as assessed in Lee et al. (2021). We more closely follow the original methods of Lee et al. (2021) in this update to base our ERF estimates as closely as possible on aviation activity data. The Lee et al. (2021) ERF time series is extended to 2019 based on aviation fuel consumption from the International Energy Agency's (IEA) World Oil Statistics (2022). For 2020, 2021 and 2022, we use fuel consumption data from the International Air Transport Association (IATA, 2022).

S4.5 Methods for estimating natural forcing

Natural forcing is composed of solar irradiance and volcanic eruptions.

S4.5.1 Solar irradiance

The method to compute solar forcing is unchanged from AR6, using a composite time series prepared for PMIP4 (Jungclaus et al., 2017) and CMIP6 (Matthes et al., 2017). The headline assessment of solar ERF is based on the most recent solar cycle (2009-2019), which is unchanged from AR6. Solar ERF estimates are computed relative to complete solar cycles encompassing the full "pre-industrial" period where proxy data exist (6754 BCE to 1745 CE).

S4.5.2 Volcanic

Volcanic ERF consists of contributions from stratospheric sulfate aerosol optical depth (sAOD; a negative forcing) and stratospheric water vapour (sWV; a positive forcing). The sAOD time series (at a nominal wavelength of 550 nm) is constructed from a combination of four datasets which have temporal overlap. We use ice-core deposition data from HolVol v1.0 (Sigl et al., 2022) for 9500 BCE to 1900 CE. These data have been extended backwards in time from the equivalent dataset used in AR6 (eVolv2k; Toohey and Sigl, 2017) which had temporal coverage of 500 BCE to 1900 CE. For 1850 to 2014 we use the CMIP6 volcanic sAOD dataset (Dhomse et al., 2020). For 1979 onwards, the CMIP6 dataset was constructed using the Global Space-based Stratospheric Aerosol Climatology (GloSSAC) v1.0 (Thomason et al., 2018). We use an updated, extended version of GloSSAC (v2.2) providing sAOD up to 2021, which is itself an extension of the version used in AR6 (v2.0) ending in 2018 (Kovilakam et al., 2020). The 525 nm extinction from GloSSAC is used and converted to 550 nm using an Ångstrom exponent of -2.33. For 2013 to 2022, we use the Ozone Mapping and Profiling Limb Profiler (OMPS LP) Level 3 aerosol optical depth at 745 nm, which is scaled to achieve the same time mean sAOD as GloSSAC in the overlapping 2013-2021 period as a single Ångstrom exponent is not suggested for this conversion. The 745 nm band is used as this is reported to be more stable than the bands closer to 550 nm from OMPS LP (Taha et al., 2021). Other than for the 2013-2021 overlap between GloSSAC v2.2 and OMPS LP in which only GloSSAC is used, we use a cross-fading approach to blend datasets in overlapping periods. Differences between datasets are minimal. sAOD is converted to a radiative effect using a scaling factor of -20 ± 5 as in AR6 (Smith et al., 2021b) that is representative of CMIP5 and CMIP6 models. Effective radiative forcing is calculated with reference to the change in this radiative effect since "pre-industrial", defined as the mean of all available years before 1750 CE. In other words, the mean of the pre-1750 period is defined as zero forcing.

The January 2022 eruption of Hunga Tonga-Hunga Ha'apai (HTHH) was an exceptional episode in that it emitted large amounts of water vapour into the stratosphere (Millán et al., 2022; Sellitto et al., 2022). Jenkins et al. (2023) determined the HTHH eruption increased volcanic ERF by +0.12 W m^{-2} due to sWV. The 2022 volcanic ERF has therefore been increased to account for this. sWV injections from other volcanic eruptions historically have been assumed to be negligible. This assumption for the whole Holocene is probably incorrect (1883 Krakatau may have also emitted substantial amounts of sWV

(Joshi and Jones, 2009)), but at present no known proxy datasets for sWV injections from volcanic eruptions before the observational era exist. After 1991 Pinatubo there was a marked increase in sWV above Colorado (40°N) that peaked and declined over a period of around three years following the eruption (Hurst et al., 2011). However, this was significantly smaller than the perturbation from HTHH (Millán et al., 2022) and may be obscured against a background of increasing sWV from a changing QBO state (Fueglistaler and Haynes, 2005), and reanalysis data show no obvious water vapour signal averaged across the tropical lower stratosphere (Dessler et al., 2014). We therefore do not adjust the volcanic ERF for sWV from 1991 Pinatubo or any other eruption.

S5. Global surface temperature

Surface temperature information on land and sea is available with low latency through WMO distribution channels, with monthly station data from a substantial number of stations reported within a few days of the end of the month. Sea-surface temperature data from ships and buoys are gathered from the Global Telecommunication System with a short delay. These are consolidated into global datasets by a number of institutions, making it feasible to report GMST updates within a few weeks of the end of the period of interest. The number of reporting locations on land with near-real time data available for reporting for the most recent periods is typically less than that available for historical data, as not all observation sites report recent data reliably, but this lower observation density only slightly increases the uncertainty in estimates of recent annual GMST compared with the past 20-30 years (Trewin et al., 2021).

The GMST assessment in AR6 was based on four datasets: HadCRUT5 (Morice et al., 2021), Berkeley Earth (Rohde and Hausfather, 2020), NOAAGlobalTemp - Interim (Vose et al., 2021) and Kadow et al. (2020). (A fifth dataset, China-MST (Sun et al., 2021), was used for the land assessment only.) The four GMST datasets were chosen by virtue of being quasi-globally complete, having data back to 1850, using the most recent generation of SST analyses and using analysed (rather than climatological) values over sea ice. The first two of these are routinely updated operationally, with data for each year becoming available in the first few weeks of the following year. NOAAGlobalTemp - Interim was not updated operationally at the time AR6 was published but has become NOAA's main operational GMST dataset (under the name NOAAGlobalTemp 5.1) as of January 2023. All three datasets are updated and published monthly. The dataset by Kadow et al. is updated on an ad hoc basis by the authors. To date, all four datasets remain supported with only minor version changes (if any) since AR6, but it is likely that more substantive version changes will occur to one or more over time, potentially leading to differences from the AR6. The key differences between the AR6 datasets and those used in the annual WMO and BAMS State of the Climate reports are that WMO and BAMS also incorporate reanalyses (ERA5 and JRA-55). These reports also include the GISTEMP (Lenssen et al., 2019) dataset (excluded by AR6 because it starts in 1880) but do not include the dataset by Kadow et al. yet (as that is not updated operationally).

The GMST values used in AR6 were calculated from the gridded datasets produced by the data providers, using a consistent methodology - calculating the mean anomaly for each of the Northern and Southern Hemisphere as a latitude-weighted mean of available grid point values and then defining the global mean anomaly as the mean of the two hemispheric values. (This is equivalent to the method used by the Met Office Hadley Centre to report global values from HadCRUT5.) The values thus calculated may differ from those reported by the data providers themselves, due to different averaging methodologies. Although the difference is less pronounced in the AR6 datasets than in earlier generations of datasets, there are more grid points with missing data in the Southern Hemisphere than the Northern Hemisphere (particularly before an observation network was established on Antarctica in the 1950s), and using hemispheric means ensures that the two hemispheres are equally weighted.

The uncertainty assessment in AR6 combines the spread of the individual datasets, with uncertainties derived from ensembles for HadCRUT5 and an earlier version of NOAAGlobalTemp, with the other two datasets assumed to have the same uncertainty as HadCRUT5. HadCRUT5 is the only one of the datasets for which regularly updated ensembles are currently produced, limiting the extent to which uncertainty assessments can be regularly updated from those used in AR6. In this update it was assumed that the width of the confidence interval for each individual dataset was the same as that used in AR6.

S7. Human-induced warming

This presents the three methods of estimating human-induced warming and describes how they have been updated since AR6 WGI.

S7.1 Global Warming Index

Introduced in Otto et al. 2015, and refined with full uncertainty assessment in Haustein et al., 2017, the Global Warming Index (GWI) quantifies anthropogenic warming by using an established "multi-fingerprinting" approach to decompose total warming into its various components; preliminary anthropogenic and natural warming time series are first estimated from radiative forcings, and a multivariate linear regression is then taken between these preliminary GMST contributions and observed GMST, with the best fit providing the attributed anthropogenic and natural contributions to warming. As such, the GWI attribution method is directly tied to observations and has a low dependence on uncertainties in climate sensitivity and forcing.

Substantive annual updates to the GWI assessment depend on annual updates for effective radiative forcings (ERFs) and observed temperature (GMST), both of which are provided as a part of this update (Sects. 4 and 5 respectively). The remaining inputs to the GWI assessment are updated at the less-frequent CMIP cadence; however these contributions only weakly influence the GWI results. Further, by recomputing a "historical-only" GWI time series based only on data up to a given year, it can be shown that GWI is relatively insensitive to end-date or short-term fluctuations in observed GMST, minimising potential confusion about the current level of warming, such as the perception of a hiatus or acceleration (see AR6 WGI Chapter 3 Cross-Chapter Box 3.1, Eyring et al., 2021), due to short-term internal variability. This, combined with the conceptual simplicity of the method, makes the GWI a relatively transparent and robust method for attributing anthropogenic warming and well-suited to providing reliable annual updates.

Where the GWI method previously separated warming contributions into two components, "anthropogenic" and "natural", and independently attributed them, this update further separates and independently attributes contributions within the Anthropogenic component, adopting the groupings from AR6: "well-mixed greenhouse gases", "other human forcings" and "natural forcings". The climate response model used to estimate (pre-regression) warming from radiative forcing is updated from the AR5 Impulse Response model (AR5-IR; from AR5 Chapter 8 Supplement (Myhre et al., 2013b)) used in Haustein et al. (2017) to the Finite-amplitude Impulse Response model (FaIR; Leach et al., 2021; Smith et al., 2018b; Millar et al., 2017), which has established use in SR1.5 and AR6; climate response uncertainty is included by using around 30 sets of parameters that correspond to FaIR emulating the CMIP6 ensemble, as provided in Leach et al. (2021). The updated historical ERF input to FaIR is given in Sect. 4, with uncertainty accounted for using a representative 1000-member probabilistic ensemble. Observed GMST and its uncertainty are provided by the 200-member ensemble of the annually updated HadCRUT5 (Morice et al. 2021; see Sect. 5). Uncertainty from internal variability is accounted for by using between 100-200 realisations of internal variability sampled from the CMIP6 piControl simulations. Since some CMIP6 models may have unrealistically high decadal variability, our estimates of uncertainty may be conservative (Erying et al., 2021). Here, to partly address this, piControl time series are first filtered, removing simulations that drift or exhibit unrealistic variability amplitudes, changing by more than 0.15 °C per decade.

Producing the GWI ensemble with ~1 billion members is computationally expensive; therefore an ensemble with ~6 million members is randomly subsampled to obtain results. Uncertainty converges at this scale, and repeat random samplings at the same scale lead to variation in the results of about 0.01°C.

S7.2 Kriging for climate change

The kriging for climate change method was originally introduced by Ribes et al. (2021), and subsequently extended in Qasmi and Ribes (2022), to attribute past warming and constrain temperature projections over the 21st century. This statistical method is very similar to snsemble Kalman filtering or kriging. In the original publication (Ribes et al., 2021), a subset of 22 CMIP6 models was used to form an a priori distribution (in a Bayesian sense) of past attributable warming. Then the posterior distribution of past attributable warming given observations was derived. This application was based on HadCRUT4-CW GMST observations (Cowtan and Way, 2014), inflated by 6% to account for stronger warming of GSAT relative to GMST. Results from this calculation were quoted in Eyring et al. (2021).

The update made here uses the same subset of 22 CMIP6 models. However, HadCRUT5 observations are used, instead of previous datasets, over an extended 1850-2022 period. Consistent with the AR6 assessment about GMST to GSAT warming ratio, no scaling correction is applied; i.e. the global mean value from HadCRUT5 is assumed to be representative of GSAT changes (see Sect. 7.1.2). As it relies on available CMIP6 simulations, this update assumes that the world has followed a SSP2-4.5 pathway since 2015. Emissions in the SSP scenarios are similar in the period up until 2022 and close to those which have occurred (e.g. Chen et al., 2021); therefore this is a reasonable approximation. Future updates with this method will incorporate new observations. In parallel, we will try to replace the CMIP6 models by emulators, thus allowing the latest available estimates of radiative forcings to be considered, instead of the SSP2-4.5 scenario.

S7.3 Regularized optimal fingerprinting

Optimal fingerprinting is the name given to optimal regression-based approaches to attribution, in which observed anomalies are regressed onto the simulated response to individual forcings from climate models, with the regression coefficients used to infer attributable contributions to observed changes (e.g. Allen and Stott, 2003; Eyring et al., 2021). Ribes et al. (2013) proposed an improved version of the standard total least squares regression, known as regularised optimal fingerprinting, which exhibited improved accuracy in perfect model tests. Gillett et al. (2021) applied this approach to regress observed 5-year mean observed GMST onto the simulated response to individual forcings from the DAMIP simulations (Gillett et al., 2016) of 13 CMIP6 models. In order to ensure a like-for-like comparison, Gillett et al. (2021) regressed observations of GMST, derived from gridded non-infilled near-surface air temperature over land and sea ice, and sea surface temperature over oceans, onto GMST derived from CMIP6 model output in the same way (Cowtan et al., 2015). However, since globally complete GSAT is usually used in the climate impact literature which served as a basis for global warming goals, Gillett et al. (2021) used regression coefficients to infer attributable warming in globally complete GSAT.

Gillett et al. (2021) used CMIP6 DAMIP simulations which generally finished in 2020 and therefore cannot directly be used to infer attributable warming in subsequent years. However, some modelling centres ran single-forcing DAMIP simulations into the future under the SSP2-4.5 scenario (Gillett et al., 2016). Data from concatenated historical and ssp245, hist-nat and ssp245-nat, and hist-GHG and ssp245-GHG were taken from CanESM5 (50, 10, 10), IPSL-CM6A-LR (11, 10, 6) and MIROC6 (3, 50, 50), where numbers in brackets indicate the respective ensemble sizes. Our approach assumes that observed drivers have evolved as in the SSP2-4.5 scenario over the period since 2015, which is a reasonable assumption to the present (e.g. Chen et al., 2021). As in Gillett et al. (2021), internal variability was estimated from intra-ensemble anomalies. Whereas the Gillett et al. (2021) results assessed by Eyring et al. (2021) were based on HadCRUT4, this dataset is no longer being updated, and therefore we use the non-infilled version of HadCRUT5 here (Morice et al., 2021). As shown by Gillett et al. (2021), using HadCRUT5 in place of HadCRUT4 results in a 7% increase in the best estimate of anthropogenic warming for 2010-2019. Gillett et al. (2021) regressed 34 5-year means of GMST over the period 1850-2019 onto simulated GMST over the same period. Here we extend the analysis using 35 5-year means, with the latter based on observations from January 2020 to February 2023 and the model output masked in the same way. In order to be consistent with the Global Warming Index and kriging for climate change approaches described above, and for comparison with GMST observations, we primarily report attributable warming in globally complete GMST here, rather than GSAT (see Sect. 7.1.2). Calculated anthropogenic warming in GSAT in 2010-2019 computed using HadCRUT5 with this approach of 1.16 (1.04-1.29) °C can be compared with the same quantity reported in Gillett et al. (2021) (their Supplementary Table 1) of 1.18 (1.09-1.27) °C, indicating good consistency.

The method described above is easily updatable into the future using the same set of simulations, simply by updating observations to a later date and masking model output accordingly. As in the KCC method, a caveat to this approach is that it relies on SSP2-4.5 simulations from which actual anthropogenic forcing might be expected to gradually diverge and from which actual natural forcing could rapidly diverge, for example, were a major volcanic eruption to occur.

Table S2: Estimates of global mean surface air temperature (GSAT) warming attributable to multiple influences (in °C) relative to the 1850–1900 baseline period. Values are given as the median, with the 5-95 percentile range in brackets, provided to 0.01°C precision. GSAT results here are only provided for regularised optimal fingerprinting (ROF) because the GSAT results for the other attribution methods (the Global Warming Index (GWI) and kriging for climate change (KCC)) are identical to the GMST results for those methods.

Component	Method	2010-2019 (decade average)	2013-2022 (decade average)	2017 (single year)	2022 (single year)
Human-induced	ROF	1.16 (1.04 to 1.29)	1.26 (1.10 to 1.41)	1.26 (1.06 to 1.41)	1.41 (1.13 to 1.69)
Well-mixed greenhouse gases		1.39 (1.14 to 1.65)	1.47 (1.20 to 1.74)	1.45 (1.15 to 1.80)	1.58 (1.25 to 1.92)

Other human forcings		-0.21 (-0.43 to 0.00)	-0.21 (-0.43 to 0.01)	-0.21 (-0.45 to 0.03)	-0.19 (-0.45 to 0.07)
Natural forcings		0.02 (0.00 to 0.03)	0.02 (-0.03 to 0.06)	0.01 (-0.05 to 0.08)	-0.01 (-0.15 to 0.12)

Table S3: Estimates of global mean surface temperature (GMST) warming attributable to multiple influences (in °C) relative to the 1850–1900 baseline period, provided for each warming attribution method and the overall multi-method assessment. Values for individual attribution methods are given as the median, with the 5-95 percentile range in brackets, provided to 0.01°C precision. Values for the assessment are calculated as defined in Sect. 7.3 and given as best estimates with *likely* ranges in brackets.

Variable	Method	2010-2019 (decadeaverage)	2013-2022 (decadeaverage)	2017 (single year)	2022 (single year)	2017 (trend-based)	2022 (trend-based)
Human-induced	GWI	1.08 (0.98 to 1.18)	1.15 (1.05 to 1.25)	1.14 (1.04 to 1.24)	1.26 (1.14 to 1.37)	1.13 (1.02 to 1.23)	1.25 (1.14 to 1.37)
	KCC	1.01 (0.86 to 1.14)	1.08 (0.92 to 1.22)	1.06 (0.91 to 1.21)	1.19 (1.02 to 1.35)	1.06 (0.91 to 1.20)	1.18 (1.02 to 1.34)
	ROF	1.11 (0.98 to 1.24)	1.19 (1.05 to 1.34)	1.18 (1.02 to 1.33)	1.34 (1.18 to 1.51)	1.15 (1.01 to 1.28)	1.33 (1.13 to 1.52)
	Assessment	1.07 (0.8 to 1.3)	1.14 (0.9 to 1.4)	1.13 (0.9 to 1.4)	1.26 (1.0 to 1.6)	1.11 (0.9 to 1.3)	1.26 (1.0 to 1.6)
Well-mixed greenhouse gases	GWI	1.25 (1.06 to 1.51)	1.31 (1.11 to 1.58)	1.30 (1.10 to 1.57)	1.40 (1.19 to 1.69)	1.30 (1.10 to 1.56)	1.40 (1.18 to 1.69)
	KCC	1.40 (1.06 to 1.71)	1.47 (1.11 to 1.79)	1.45 (1.10 to 1.78)	1.56 (1.18 to 1.92)	1.45 (1.10 to 1.78)	1.56 (1.18 to 1.92)
	ROF	1.34 (1.11 to 1.56)	1.41 (1.17 to 1.65)	1.39 (1.15 to 1.64)	1.51 (1.26 to 1.77)	1.38 (1.15 to 1.62)	1.51 (1.25 to 1.76)
	Assessment	1.33 (1.0 to 1.8)	1.40 (1.1 to 1.8)	1.38 (1.1 to 1.8)	1.49 (1.1 to 2.0)	1.38 (1.0 to 1.8)	1.49 (1.1 to 2.0)
Other human forcings	GWI	-0.17 (-0.42 to 0.02)	-0.16 (-0.41 to 0.03)	-0.16 (-0.41 to 0.03)	-0.14 (-0.39 to 0.04)	-0.17 (-0.42 to 0.02)	-0.14 (-0.39 to 0.05)
	KCC	-0.39 (-0.68 to -0.10)	-0.39 (-0.68 to -0.09)	-0.39 (-0.69 to -0.09)	-0.38 (-0.68 to -0.06)	-0.39 (-0.69 to -0.09)	-0.38 (-0.69 to -0.07)
	ROF	-0.21 (-0.41 to 0.00)	-0.20 (-0.41 to 0.00)	-0.20 (-0.41 to 0.00)	-0.19 (-0.38 to 0.00)	-0.21 (-0.43 to 0.00)	-0.19 (-0.40 to 0.01)
	Assessment	-0.26 (-0.7 to 0.1)	-0.25 (-0.7 to 0.1)	-0.25 (-0.7 to 0.1)	-0.24 (-0.7 to 0.1)	-0.26 (-0.7 to 0.1)	-0.24 (-0.7 to 0.1)
Natural forcings	GWI	0.06 (0.03 to 0.10)	0.06 (0.03 to 0.10)	0.06 (0.03 to 0.10)	0.05 (0.02 to 0.09)	0.06 (0.03 to 0.10)	0.06 (0.03 to 0.10)
	KCC	0.06 (0.04 to 0.08)	0.06 (0.04 to 0.07)	0.06 (0.04 to 0.08)	0.04 (0.03 to 0.06)	0.06 (0.04 to 0.08)	0.05 (0.03 to 0.07)
	ROF	0.02 (-0.02 to 0.05)	0.02 (-0.02 to 0.06)	0.01 (-0.03 to 0.06)	-0.01 (-0.07 to 0.04)	0.02 (-0.02 to 0.05)	0.01 (-0.03 to 0.06)
	Assessment	0.05 (-0.1 to 0.1)	0.04 (-0.1 to 0.1)	0.04 (-0.1 to 0.2)	0.03 (-0.1 to 0.1)	0.05 (-0.1 to 0.1)	0.04 (-0.1 to 0.1)

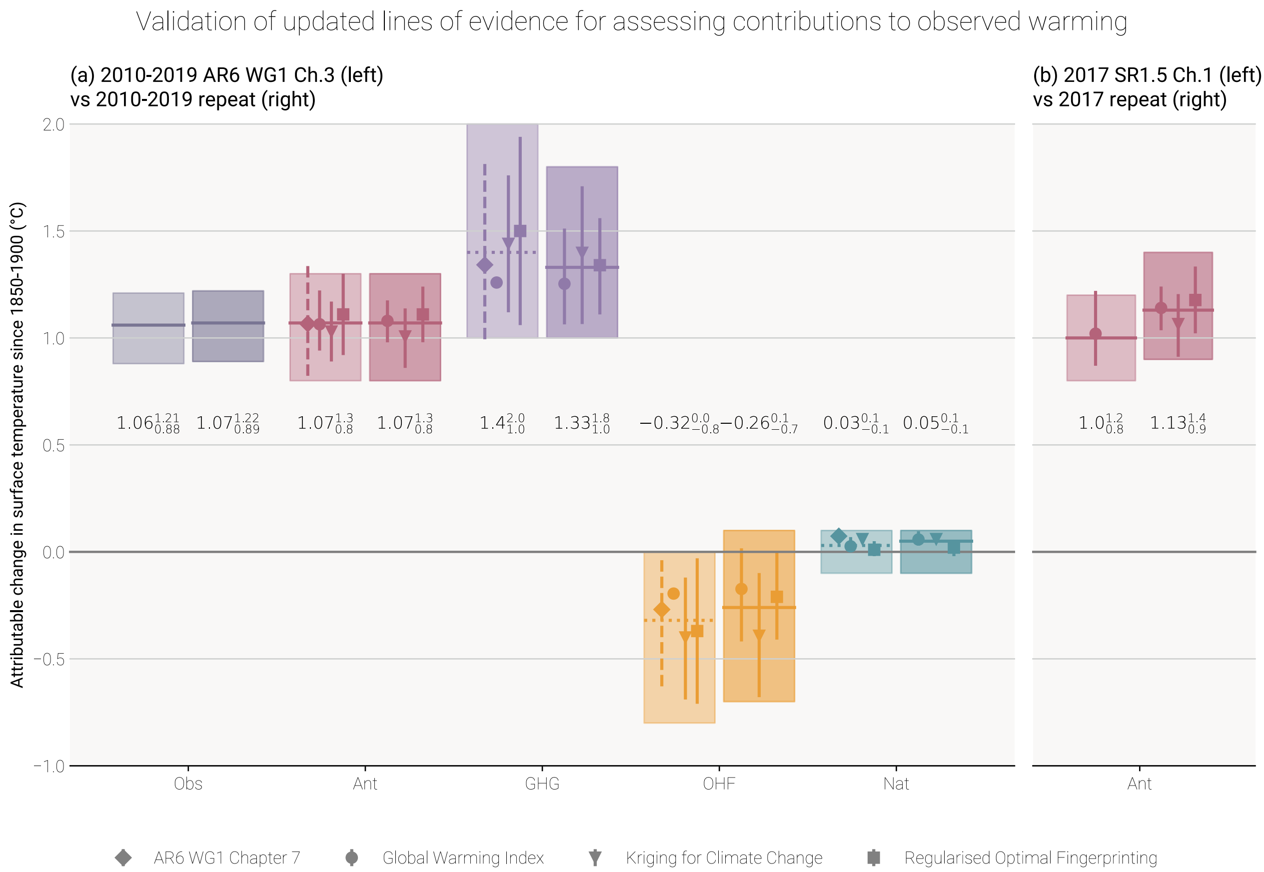

Figure S1: Assessed contributions to observed warming and supporting lines of evidence; see AR6 WG1 Figure 3.8. The shaded bands show assessed likely ranges of temperature change, relative to the 1850-1900 baseline, attributable to total anthropogenic influence (Ant), well-mixed greenhouse gases (GHGs), other human forcings (OHFs), and natural forcings (Nat). The left of each pair of bands depicts the results quoted from AR6, and the right of each pair of bands depicts a repeat calculation for the same period as the IPCC assessment, using the revised datasets and methods, to validate the updated assessment of attributable warming. Panel (a) presents decade-average warming as used in AR6, with results quoted from AR6 WGI Chapter 3 on the left and the repeat assessment on the right. The solid horizontal bar in each band shows the best estimate for each warming component; if no best estimate was provided, it was retrospectively calculated using the AR6 method and depicted using a horizontal dotted line to facilitate comparison. In AR6, Global Warming Index results were reported as GMST, kriging for climate change results were calculated as GMST and scaled by 1.06 for reporting as GSAT, and regularised optimal fingerprinting was reported as GSAT; for the repeat, all methods are reported in terms of GMST (see Sect. 7.1.2 for discussion). Panel (b) presents single-year warming as used in SR1.5, with results quoted from SR1.5 Chapter 1 on the left (which was based only on the GWI) and the repeat assessment on the right, which now includes all of the attribution methods and the multi-method assessment approach used in AR6, as discussed in Sect. 7.3.2. Both bars are reported in GMST. No assessment was provided for components other than Ant in SR1.5.

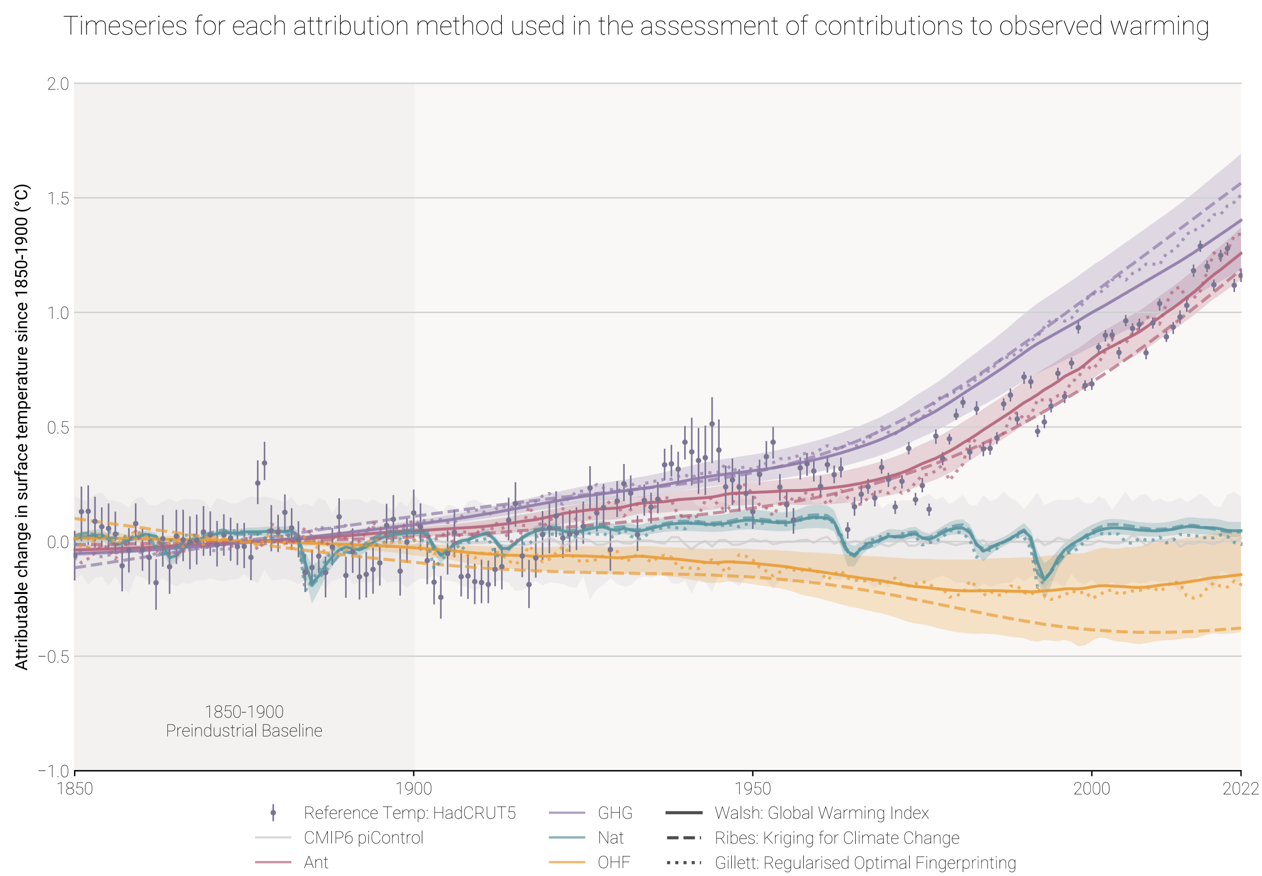

Figure S2: Time series for each attribution method used in the updated assessment of warming contributions, expressed in terms of global mean surface temperature (GMST). Coloured plumes correspond to warming contributions broken down by natural forcings (Nat), well-mixed greenhouse gases (GHGs) and other human forcings (OHFs). Total human-induced warming (Ant) is therefore the sum of contributions from GHG and OHF. The plume range is given by the 5-95% range of the Global Warming Index (GWI), with the GWI best estimate given by the solid lines. The dashed line presents the best estimate from the kriging for climate change (KCC) method, and the dotted line presents the best estimate from the regularised optimal fingerprinting (ROF) method. GWI and KCC are given as annual values based on infilled GMST from HadCRUT5; ROF is given as annual values of globally complete GMST. The CMIP6 pre-industrial control (piControl) simulations are used as a proxy for multiple samplings of internal variability and are used to account for attribution uncertainty resulting from internal variability in the GWI method (see Supplementary Sect. 7.1).

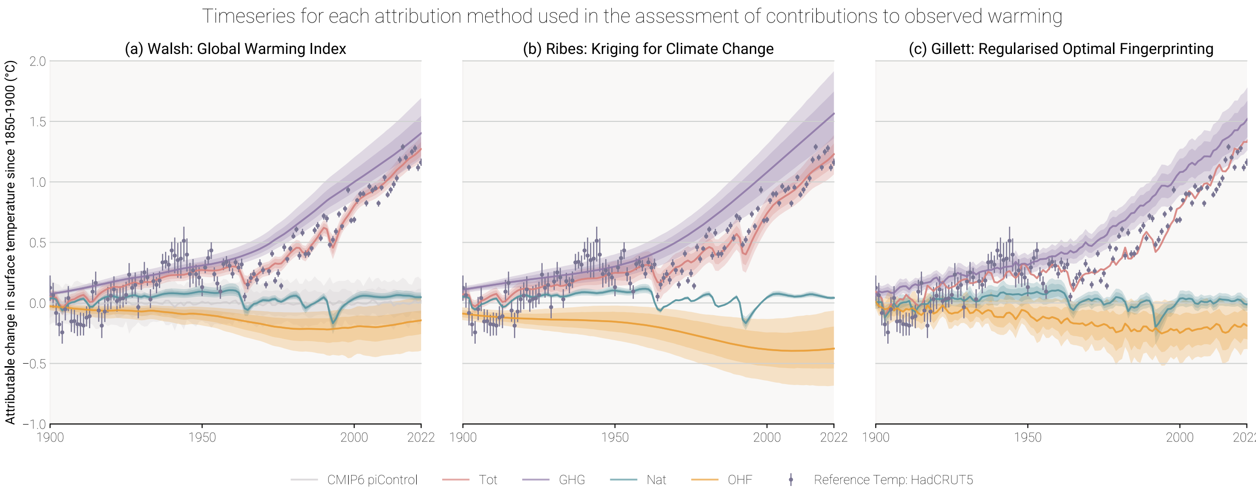

Figure S3: Time series for each attribution method used in the updated assessment of warming contributions, expressed in terms of global mean surface temperature (GMST). Coloured plumes are given for both 17-83% and 5-95% ranges and correspond to warming contributions to observed warming broken down by natural forcings (Nat), well-mixed greenhouse gases (GHGs) and other human forcings (OHFs). Total warming (Tot) is the total attributable warming and therefore the sum of contributions from GHG, OHF and Nat. Observation data from (infilled) HadCRUT5 are presented with 9-95% uncertainty bars. Panel (a) presents results from the Global Warming Index method (Supplementary Sect. 7.1); the CMIP6 pre-industrial control (piControl) simulations are used as a proxy for multiple samplings of internal variability and used to account for uncertainty in the attribution resulting from internal variability (see Supplementary Sect. 7.1). Panel (b) presents results from the kriging for climate change methods (Supplementary Sect. 7.2). Panel (c) presents results from regularised optimal fingerprinting (Supplementary Sect. 7.3), with the time series for Tot being approximated by the sum of the Ant and Nat medians; note that this is different from GWI and KCC, where Tot is an attributed quantity.

The results for each individual methods are available in csv form in the Climate Indicator repository: https://github.com/ClimateIndicator/anthropogenic-warming-assessment/.

S8. Remaining carbon budget

Estimating the remaining carbon budget (RCB) requires an estimate of future non-CO_2 warming. The latter estimate is derived from the emissions trajectories as modelled by internally consistent emissions scenarios. While RCB estimates are for CO_2 emissions only, the consideration of non-CO_2 warming implies that assumptions are also made about reductions in other anthropogenic forcers. These reductions have to be kept in mind, as a shortfall in non-CO_2 greenhouse gas emissions would result in a smaller RCB estimate. For instance, the estimate of RCBs consistent with limiting warming to 1.5°C assumes a median reduction in CH_4 emissions between 2020 and 2050 of about 50% (while the interquartile range across available scenarios is 45–58%), about a 25% reduction between 2020 and 2050 in N_2O emissions (interquartile range: 7–35%), and a 77% reduction between 2020 and 2050 in SO_2 emissions (interquartile range: 75–79%). Assumed reductions consistent with other levels of warming are provided in Table S2. The estimates reported in Table 7 of the main paper are based on the median non-CO_2 emission reductions. Falling short of achieving the assumed non-CO_2 greenhouse gas emissions reductions would further reduce the RCB. Sulfur dioxide emissions are more tightly co-controlled with CO_2 reduction because of the phase-out of unabated fossil fuel combustion and air pollution control measures (Rogelj et al., 2014a, 2014b). A shortfall in their reductions would therefore be less conceivable in a net-zero CO_2 world.

Table S4: Non-CO_2 reductions implied in remaining carbon budget (RCB) estimates. Values represent the changes in non-CO_2 emissions between 2020 and 2050, consistent with the RCB estimates for 1.5°C, 1.7°C and 2.0°C. The median changes are the default and marked in light blue. Any deviation from this median assumption results in an increase or decrease of the RCB estimate.

Temperature level for which RCB was estimated	**Percentile**	**Implied non-CO_2 change between 2020 and 2050 [%]**		
		CH_4	**N_2O**	**SO_2**
1.5°C	**10th**	-64	-47	-84
	25th	-58	-35	-79
	50th	-48	-25	-77
	75th	-45	-7	-75
	90th	-41	-4	-65
1.7°C	**10th**	-63	-44	-79
	25th	-53	-29	-77
	50th	-47	-15	-75
	75th	-42	-8	-71
	90th	-35	-4	-65
2.0°C	**10th**	-54	-37	-76
	25th	-47	-24	-74
	50th	-35	-9	-68
	75th	-27	-1	-60
	90th	-18	+5	-52

S9. Examples of climate and weather extremes: maximum temperature over land

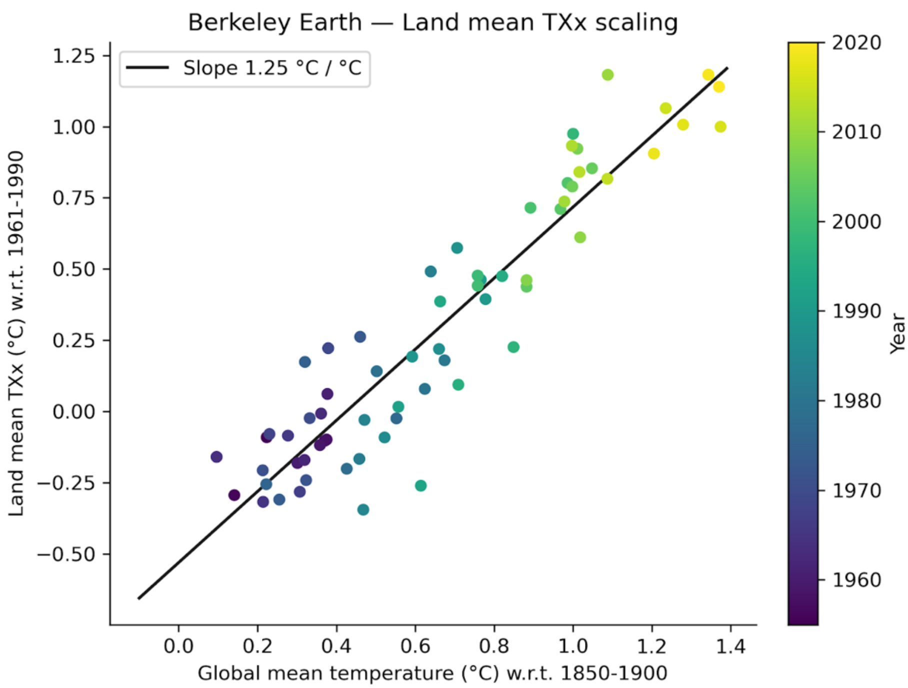

Figure S4: Calculation of land mean annual maximum temperature (TXx) offset between 1850-1900 and 1961-1990. A linear regression of TXx as a function of global mean temperature from Berkeley Earth is fitted to data from 1955-2020. The TXx offset of 0.53 °C is then obtained by multiplying the slope of the linear regression (1.25 °C / °C) with the global mean temperature difference between 1850-1900 and 1961-1990 (0.43°C).

References

Allen, M. R. and Stott, P. A.: Estimating signal amplitudes in optimal fingerprinting, part I: theory, Climate Dynamics, 21, 477–491, https://doi.org/10.1007/s00382-003-0313-9, 2003.

Chen, D., M. Rojas, B. H. Samset, K. Cobb, A. Diongue Niang, P. Edwards, S. Emori, S. H. Faria, E. Hawkins, P. Hope, P. Huybrechts, M. Meinshausen, S. K. Mustafa, G.-K. Plattner, and A.-M. Tréguier, 2021: Framing, Context, and Methods. In Climate Change 2021: The Physical Science Basis. Contribution of Working Group I to the Sixth Assessment Report of the Intergovernmental Panel on Climate Change [Masson-Delmotte, V., P. Zhai, A. Pirani, S. L. Connors, C. Péan, S. Berger, N. Caud, Y. Chen, L. Goldfarb, M. I. Gomis, M. Huang, K. Leitzell, E. Lonnoy, J. B. R. Matthews, T. K. Maycock, T. Waterfield,

O. Yelekçi, R. Yu, and B. Zhou (eds.)]. Cambridge University Press, Cambridge, United Kingdom and New York, NY, USA, pp. 147–286, https://doi.org/:10.1017/9781009157896.003, 2021.

Cowtan, K. and Way, R. G.: Coverage bias in the HadCRUT4 temperature series and its impact on recent temperature trends, Q.J.R. Meteorol. Soc., 140, 1935–1944, https://doi.org/10.1002/qj.2297, 2014.

Cowtan, K., Hausfather, Z., Hawkins, E., Jacobs, P., Mann, M. E., Miller, S. K., Steinman, B. A., Stolpe, M. B., and Way, R. G.: Robust comparison of climate models with observations using blended land air and ocean sea surface temperatures, Geophys. Res. Lett., 42, 6526–6534, https://doi.org/10.1002/2015GL064888, 2015.

Dessler, A. E., Schoeberl, M. R., Wang, T., Davis, S. M., Rosenlof, K. H., and Vernier, J.-P.: Variations of stratospheric water vapor over the past three decades, J. Geophys. Res.-Atmos., 119, 12588-12598, https://doi.org/10.1002/2014JD021712, 2014.

Dhomse, S. S., Mann, G. W., Antuña Marrero, J. C., Shallcross, S. E., Chipperfield, M. P., Carslaw, K. S., Marshall, L., Abraham, N. L., and Johnson, C. E.: Evaluating the simulated radiative forcings, aerosol properties, and stratospheric warmings from the 1963 Mt Agung, 1982 El Chichón, and 1991 Mt Pinatubo volcanic aerosol clouds, Atmos. Chem. Phys., 20, 13627–13654, https://doi.org/10.5194/acp-20-13627-2020, 2020.

Etminan, M., Myhre, G., Highwood, E. J., and Shine, K. P.: Radiative forcing of carbon dioxide, methane, and nitrous oxide: A significant revision of the methane radiative forcing, Geophys. Res. Lett., 43, 12614-12623, https://doi.org/10.1002/2016GL071930, 2016.

Eyring, V., N. P. Gillett, K.M. Achuta Rao, R. Barimalala, M. Barreiro Parrillo, N. Bellouin, C. Cassou, P. J. Durack, Y. Kosaka, S. McGregor, S. Min, O. Morgenstern, and Y. Sun: Human Influence on the Climate System. In Climate Change 2021: The Physical Science Basis. Contribution of Working Group I to the Sixth Assessment Report of the Intergovernmental Panel on Climate Change[Masson-Delmotte, V., P. Zhai, A. Pirani, S.L. Connors, C. Péan, S. Berger, N. Caud, Y. Chen, L. Goldfarb, M.I. Gomis, M. Huang, K. Leitzell, E. Lonnoy, J.B.R. Matthews, T.K. Maycock, T. Waterfield, O. Yelekçi, R. Yu, and B. Zhou (eds.)]. Cambridge University Press, Cambridge, United Kingdom and New York, NY, USA, pp. 423–552, http://doi:10.1017/9781009157896.005, 2021.

Fueglistaler, S. and Haynes, P. H.: Control of interannual and longer-term variability of stratospheric water vapor, J. Geophys. Res., 110, D24108, https://doi.org/10.1029/2005JD006019, 2005.

Gillett, N. P., Shiogama, H., Funke, B., Hegerl, G., Knutti, R., Matthes, K., Santer, B. D., Stone, D., and Tebaldi, C.: The Detection and Attribution Model Intercomparison Project (DAMIP v1.0) contribution to CMIP6, Geosci. Model. Dev., 9, 3685–3697, https://doi.org/10.5194/gmd-9-3685-2016, 2016.

Gillett, N.P., Kirchmeier-Young, M., Ribes, A., Shiogama, H., Hegerl, G.C., Knutti, R., Gastineau, G., John, J.G., Li, L., Nazarenko, L., Rosenbloom, N., Seland, Ø., Wu, T., Yukimoto, S., and Ziehn, T.: Constraining human contributions to observed warming since the pre-industrial period, Nat. Clim. Chang., 11, 207–212, https://doi.org/10.1038/s41558-020-00965-9, 2021.

Gulev, S. K., P. W. Thorne, J. Ahn, F. J. Dentener, C. M. Domingues, S. Gerland, D. Gong, D. S. Kaufman, H. C. Nnamchi, J. Quaas, J.A. Rivera, S. Sathyendranath, S.L. Smith, B. Trewin, K. von Schuckmann, and R. S. Vose: Changing State of the Climate System. In Climate Change 2021: The Physical Science Basis. Contribution of Working Group I to the Sixth Assessment Report of the Intergovernmental Panel on Climate Change[Masson-Delmotte, V., P. Zhai, A. Pirani, S.L. Connors, C. Péan, S. Berger, N. Caud, Y. Chen, L. Goldfarb, M.I. Gomis, M. Huang, K. Leitzell, E. Lonnoy, J.B.R. Matthews, T.K. Maycock, T. Waterfield, O. Yelekçi, R. Yu, and B. Zhou (eds.)]. Cambridge University Press, Cambridge, United Kingdom and New York, NY, USA, pp. 287–422, https://doi.org/10.1017/9781009157896.004, 2021.

Haustein, K., Allen, M. R., Forster, P. M., Otto, F. E. L., Mitchell, D. M., Matthews, H. D., and Frame, D. J.: A real-time Global Warming Index, Sci Rep, 7, 15417, https://doi.org/10.1038/s41598-017-14828-5, 2017.

Hodnebrog, Ø., Myhre, G., Kramer, R. J., Shine, K. P., Andrews, T., Faluvegi, G., Kasoar, M., Kirkevåg, A., Lamarque, J.-F., Mülmenstädt, J., Olivié, D., Samset, B. H., Shindell, D., Smith, C. J., Takemura, T., and Voulgarakis, A.: The effect of rapid adjustments to halocarbons and N2O on radiative forcing, npj Clim. Atmos. Sci., 3, 43, https://doi.org/10.1038/s41612-020-00150-x, 2020a.

Hodnebrog, Ø., Aamaas, B., Fuglestvedt, J. S., Marston, G., Myhre, G., Nielsen, C. J., Sandstad, M., Shine, K. P., and Wallington, T. J.: Updated Global Warming Potentials and Radiative Efficiencies of Halocarbons and Other Weak Atmospheric Absorbers, Rev. Geophys., 58, e2019RG000691, https://doi.org/10.1029/2019RG000691, 2020b.

Hurst, D. F., Oltmans, S. J., Vömel, H., Rosenlof, K. H., Davis, S. M., Ray, E. A., Hall, E. G., and Jordan, A. F.: Stratospheric water vapor trends over Boulder, Colorado: Analysis of the 30 year Boulder record, J. Geophys. Res.-Atmos., 116, https://doi.org/10.1029/2010JD015065, 2011.

IATA: Global Outlook for Air Transport: Times of Turbulence, IATA, https://www.iata.org/en/iata-repository/publications/economic-reports/airline-industry-economic-performance---june-2022---report/, 2022.

IEA: World oil statistics (Edition 2021), IEA Oil Information Statistics (database), https://doi.org/10.1787/558987b9-en, 2022 (accessed on 24 April 2023).

Jenkins, S., Smith, C., Allen, M., and Grainger, R.: Tonga eruption increases chance of temporary surface temperature anomaly above 1.5 °C, Nature Clim. Chang., 13, 127–129, https://doi.org/10.1038/s41558-022-01568-2, 2023.

Joshi, M. M. and Jones, G. S.: The climatic effects of the direct injection of water vapour into the stratosphere by large volcanic eruptions, Atmos. Chem. Phys., 9, 6109–6118, https://doi.org/10.5194/acp-9-6109-2009, 2009.

Jungclaus, J. H., Bard, E., Baroni, M., Braconnot, P., Cao, J., Chini, L. P., Egorova, T., Evans, M., González-Rouco, J. F., Goosse, H., Hurtt, G. C., Joos, F., Kaplan, J. O., Khodri, M., Klein Goldewijk, K., Krivova, N., LeGrande, A. N., Lorenz, S. J., Luterbacher, J., Man, W., Maycock, A. C., Meinshausen, M., Moberg, A., Muscheler, R., Nehrbass-Ahles, C., Otto-Bliesner, B. I., Phipps, S. J., Pongratz, J., Rozanov, E., Schmidt, G. A., Schmidt, H., Schmutz, W., Schurer, A., Shapiro, A. I., Sigl, M., Smerdon, J. E., Solanki, S. K., Timmreck, C., Toohey, M., Usoskin, I. G., Wagner, S., Wu, C.-J., Yeo, K. L., Zanchettin, D., Zhang, Q., and Zorita, E.: The PMIP4 contribution to CMIP6 – Part 3: The last millennium, scientific objective, and experimental design for the PMIP4 past1000 simulations, Geosci. Model Dev., 10, 4005–4033, https://doi.org/10.5194/gmd-10-4005-2017, 2017.

Kadow, C., Hall, D. M., and Ulbrich, U.: Artificial intelligence reconstructs missing climate information, Nat. Geosci., 13, 408–413, https://doi.org/10.1038/s41561-020-0582-5, 2020.

Keeble, J., Hassler, B., Banerjee, A., Checa-Garcia, R., Chiodo, G., Davis, S., Eyring, V., Griffiths, P. T., Morgenstern, O., Nowack, P., Zeng, G., Zhang, J., Bodeker, G., Burrows, S., Cameron-Smith, P., Cugnet, D., Danek, C., Deushi, M., Horowitz, L. W., Kubin, A., Li, L., Lohmann, G., Michou, M., Mills, M. J., Nabat, P., Olivié, D., Park, S., Seland, Ø., Stoll, J., Wieners, K.-H., and Wu, T.: Evaluating stratospheric ozone and water vapour changes in CMIP6 models from 1850 to 2100, Atmos. Chem. Phys., 21, 5015–5061, https://doi.org/10.5194/acp-21-5015-2021, 2021.

Kovilakam, M., Thomason, L. W., Ernest, N., Rieger, L., Bourassa, A., and Millán, L.: The Global Space-based Stratospheric Aerosol Climatology (version 2.0): 1979–2018, Earth Syst. Sci. Data, 12, 2607–2634, https://doi.org/10.5194/essd-12-2607-2020, 2020.

Leach, N. J., Jenkins, S., Nicholls, Z., Smith, C. J., Lynch, J., Cain, M., Walsh, T., Wu, B., Tsutsui, J., and Allen, M. R.: FaIRv2.0.0: a generalized impulse response model for climate uncertainty and future scenario exploration, Geosci. Model Dev., 14, 3007–3036, https://doi.org/10.5194/gmd-14-3007-2021, 2021.

Lee, D. S., Fahey, D. W., Skowron, A., Allen, M. R., Burkhardt, U., Chen, Q., Doherty, S. J., Freeman, S., Forster, P. M., Fuglestvedt, J., Gettelman, A., León, R. R. D., Lim, L. L., Lund, M. T., Millar, R. J., Owen, B., Penner, J. E., Pitari, G., Prather, M. J., Sausen, R., and Wilcox, L. J.: The contribution of global aviation to anthropogenic climate forcing for 2000 to 2018, Atmos. Environ., 244, 117834, https://doi.org/10.1016/j.atmosenv.2020.117834, 2021.

Lenssen, N. J. L., Schmidt, G. A., Hansen, J. E., Menne, M. J., Persin, A., Ruedy, R., and Zyss, D.: Improvements in the GISTEMP Uncertainty Model, J. Geophys. Res.-Atmos., 124, 6307–6326, https://doi.org/10.1029/2018JD029522, 2019.

Matthes, K., Funke, B., Andersson, M. E., Barnard, L., Beer, J., Charbonneau, P., Clilverd, M. A., Dudok de Wit, T., Haberreiter, M., Hendry, A., Jackman, C. H., Kretzschmar, M., Kruschke, T., Kunze, M., Langematz, U., Marsh, D. R., Maycock, A. C., Misios, S., Rodger, C. J., Scaife, A. A., Seppälä, A., Shangguan, M., Sinnhuber, M., Tourpali, K., Usoskin, I., van de Kamp, M., Verronen, P. T., and Versick, S.: Solar forcing for CMIP6 (v3.2), Geosci. Model Dev., 10, 2247–2302, https://doi.org/10.5194/gmd-10-2247-2017, 2017.

Meinshausen, M., Nicholls, Z. R. J., Lewis, J., Gidden, M. J., Vogel, E., Freund, M., Beyerle, U., Gessner, C., Nauels, A., Bauer, N., Canadell, J. G., Daniel, J. S., John, A., Krummel, P. B., Luderer, G., Meinshausen, N., Montzka, S. A., Rayner, P. J., Reimann, S., Smith, S. J., van den Berg, M., Velders, G. J. M., Vollmer, M. K., and Wang, R. H. J.: The shared socio-economic pathway (SSP) greenhouse gas concentrations and their extensions to 2500, Geosci. Model Dev., 13, 3571–3605, https://doi.org/10.5194/gmd-13-3571-2020, 2020.

Millán, L., Santee, M. L., Lambert, A., Livesey, N. J., Werner, F., Schwartz, M. J., Pumphrey, H. C., Manney, G. L., Wang, Y., Su, H., Wu, L., Read, W. G., and Froidevaux, L.: The Hunga Tonga-Hunga Ha'apai Hydration of the Stratosphere, Geophys. Res. Lett., 49, e2022GL099381, https://doi.org/10.1029/2022GL099381, 2022.

Millar, R. J., Nicholls, Z. R., Friedlingstein, P., and Allen, M. R.: A modified impulse-response representation of the global near-surface air temperature and atmospheric concentration response to carbon dioxide emissions, Atmos. Chem. Phys., 17, 7213–7228, https://doi.org/10.5194/acp-17-7213-2017, 2017.

Morice, C. P., Kennedy, J. J., Rayner, N. A., Winn, J. P., Hogan, E., Killick, R. E., Dunn, R. J. H., Osborn, T. J., Jones, P. D., and Simpson, I. R.: An Updated Assessment of Near-Surface Temperature Change From 1850: The HadCRUT5 Data Set, J. Geophys. Res.-Atmos., 126, e2019JD032361, https://doi.org/10.1029/2019JD032361, 2021.

Myhre, G., Samset, B. H., Schulz, M., Balkanski, Y., Bauer, S., Berntsen, T. K., Bian, H., Bellouin, N., Chin, M., Diehl, T., Easter, R. C., Feichter, J., Ghan, S. J., Hauglustaine, D., Iversen, T., Kinne, S., Kirkevåg, A., Lamarque, J.-F., Lin, G., Liu, X., Lund, M. T., Luo, G., Ma, X., van Noije, T., Penner, J. E., Rasch, P. J., Ruiz, A., Seland, Ø., Skeie, R. B., Stier, P., Takemura, T., Tsigaridis, K., Wang, P., Wang, Z., Xu, L., Yu, H., Yu, F., Yoon, J.-H., Zhang, K., Zhang, H., and Zhou, C.: Radiative forcing of the direct aerosol effect from AeroCom Phase II simulations, Atmos. Chem. Phys., 13, 1853–1877, https://doi.org/10.5194/acp-13-1853-2013, 2013a.

Myhre, G., D. Shindell, F.-M. Bréon, W. Collins, J. Fuglestvedt, J. Huang, D. Koch, J.-F. Lamarque, D. Lee, B. Mendoza, T. Nakajima, A. Robock, G. Stephens, T. Takemura and H. Zhang: Anthropogenic and Natural Radiative Forcing. In: Climate Change 2013: The Physical Science Basis. Contribution of Working Group I to the Fifth Assessment Report of the Intergovernmental Panel on Climate Change, edited by Stocker, T.F., D. Qin, G.-K. Plattner, M. Tignor, S.K. Allen, J. Boschung, A. Nauels, Y. Xia, V. Bex and P.M. Midgley (eds.)]. Cambridge University Press, Cambridge, United Kingdom and New York, NY, USA, https://doi.org/10.1017/CBO9781107415324.018, 2013b.

Otto, F. E. L., Frame, D. J., Otto, A., and Allen, M. R.: Embracing uncertainty in climate change policy, Nature Clim. Chang., 5, 917–920, https://doi.org/10.1038/nclimate2716, 2015.

Qasmi, S. and Ribes, A.: Reducing uncertainty in local temperature projections, Sci. Adv., 8, eabo6872, https://doi.org/10.1126/sciadv.abo6872, 2022.

Ribes, A., Planton, S., and Terray, L.: Application of regularised optimal fingerprinting to attribution. Part I: method, properties and idealised analysis, Clim. Dyn., 41, 2817–2836, https://doi.org/10.1007/s00382-013-1735-7, 2013.

Ribes, A., Qasmi, S., and Gillett, N. P.: Making climate projections conditional on historical observations, Sci. Adv., 7, eabc0671, https://doi.org/10.1126/sciadv.abc0671, 2021.

Rogelj, J., Schaeffer, M., Meinshausen, M., Shindell, D. T., Hare, W., Klimont, Z., Velders, G. J., Amann, M., and Schellnhuber, H. J.: Disentangling the effects of CO2 and short-lived climate forcer mitigation, Proc. Natl. Acad. Sci. USA, 111 (46), 16325–16330, https://doi.org/10.1073/pnas.1415631111, 2014a.

Rogelj, J., Rao, S., McCollum, D. L., Pachauri, S., Klimont, Z., Krey, V., and Riahi, K: Air-pollution emission ranges consistent with the representative concentration pathways, Nature Clim. Chang., 4 (6), 446–450, https://doi.org/10.1038/nclimate2178, 2014b.

Rohde, R. A. and Hausfather, Z.: The Berkeley Earth Land/Ocean Temperature Record, Earth Sys. Sci. Data, 12, 3469–3479, https://doi.org/10.5194/essd-12-3469-2020, 2020.

Sellitto, P., Podglajen, A., Belhadji, R., Boichu, M., Carboni, E., Cuesta, J., Duchamp, C., Kloss, C., Siddans, R., Bègue, N., Blarel, L., Jegou, F., Khaykin, S., Renard, J.B., Legras, B.: The unexpected radiative impact of the Hunga Tonga eruption of 15th January 2022, Commun. Earth. Environ., 3, 288, https://doi.org/10.1038/s43247-022-00618-z, 2022.

Sigl, M., Toohey, M., McConnell, J. R., Cole-Dai, J., and Severi, M.: Volcanic stratospheric sulfur injections and aerosol optical depth during the Holocene (past 11\,500 years) from a bipolar ice-core array, Earth Syst. Sci. Data, 14, 3167–3196, https://doi.org/10.5194/essd-14-3167-2022, 2022.

Skeie, R. B., Myhre, G., Hodnebrog, Ø., Cameron-Smith, P. J., Deushi, M., Hegglin, M. I., Horowitz, L. W., Kramer, R. J., Michou, M., Mills, M. J., Olivié, D. J. L., Connor, F. M. O., Paynter, D., Samset, B. H., Sellar, A., Shindell, D., Takemura, T., Tilmes, S., and Wu, T.: Historical total ozone radiative forcing derived from CMIP6 simulations, npj Clim. Atmos. Sci., 3, 32, https://doi.org/10.1038/s41612-020-00131-0, 2020.

Smith, C. J., Kramer, R. J., Myhre, G., Forster, P. M., Soden, B. J., Andrews, T., Boucher, O., Faluvegi, G., Fläschner, D., Hodnebrog, Ø., Kasoar, M., Kharin, V., Kirkevåg, A., Lamarque, J.-F., Mülmenstädt, J., Olivié, D., Richardson, T., Samset, B. H., Shindell, D., Stier, P., Takemura, T., Voulgarakis, A., and Watson-Parris, D.: Understanding Rapid Adjustments to Diverse Forcing Agents, Geophys. Res. Lett., 45, 12,023-12,031, https://doi.org/10.1029/2018GL079826, 2018a.

Smith, C. J., Forster, P. M., Allen, M., Leach, N., Millar, R. J., Passerello, G. A., and Regayre, L. A.: FAIR v1.3: A simple emissions-based impulse response and carbon cycle model, Geoscientific Model Development, 11, 2273–2297, https://doi.org/10.5194/gmd-11-2273-2018, 2018b.

Smith, C. J., Harris, G. R., Palmer, M. D., Bellouin, N., Collins, W., Myhre, G., Schulz, M., Golaz, J.-C., Ringer, M., Storelvmo, T., and Forster, P. M.: Energy Budget Constraints on the Time History of Aerosol Forcing and Climate Sensitivity, Journal of Geophysical Research: Atmospheres, 126, e2020JD033622, https://doi.org/10.1029/2020JD033622, 2021a.

Smith, C., Nicholls, Z. R. J., Armour, K., Collins, W., Forster, P., Meinshausen, M., Palmer, M. D., and Watanabe, M.: The Earth's Energy Budget, Climate Feedbacks, and Climate Sensitivity Supplementary Material, in: Climate Change 2021: The Physical Science Basis. Contribution of Working Group I to the Sixth Assessment Report of the Intergovernmental Panel on Climate Change, edited by: Masson-Delmotte, V., Zhai, P., Pirani, A., Connors, S. L., Péan, C., Berger, S., Caud, N., Chen, Y., Goldfarb, L., Gomis, M. I., Huang, M., Leitzell, K., Lonnoy, E., Matthews, J. B. R., Maycock, T. K., Waterfield, T., Yelekçi, O., Yu, R., and Zhou, B., 2021b.

Stevenson, D. S., Young, P. J., Naik, V., Lamarque, J.-F., Shindell, D. T., Voulgarakis, A., Skeie, R. B., Dalsoren, S. B., Myhre, G., Berntsen, T. K., Folberth, G. A., Rumbold, S. T., Collins, W. J., MacKenzie, I. A., Doherty, R. M., Zeng, G., van Noije, T. P. C., Strunk, A., Bergmann, D., Cameron-Smith, P., Plummer, D. A., Strode, S. A., Horowitz, L., Lee, Y. H., Szopa, S., Sudo, K., Nagashima, T., Josse, B., Cionni, I., Righi, M., Eyring, V., Conley, A., Bowman, K. W., Wild, O., and Archibald, A.: Tropospheric ozone changes, radiative forcing and attribution to emissions in the Atmospheric Chemistry and Climate Model Intercomparison Project (ACCMIP), Atmos. Chem. Phys., 13, 3063–3085, https://doi.org/10.5194/acp-13-3063-2013, 2013.

Sun, W., Li, Q., Huang, B., Cheng, J., Song, Z., Li, H., Dong, W., Zhai, P., and Jones, P.: The Assessment of Global Surface Temperature Change from 1850s: The C-LSAT2.0 Ensemble and the CMST-Interim Datasets, Advances in Atmospheric Sciences, 38, 875–888, https://doi.org/10.1007/s00376-021-1012-3, 2021.

Szopa, S., V. Naik, B. Adhikary, P. Artaxo, T. Berntsen, W.D. Collins, S. Fuzzi, L. Gallardo, A. Kiendler-Scharr, Z. Klimont, H. Liao, N. Unger, and P. Zanis: Short-Lived Climate Forcers. In Climate Change 2021: The Physical Science Basis. Contribution of Working Group I to the Sixth Assessment Report of the Intergovernmental Panel on Climate Change [Masson-Delmotte, V., P. Zhai, A. Pirani, S.L. Connors, C. Péan, S. Berger, N. Caud, Y. Chen, L. Goldfarb, M.I. Gomis, M. Huang, K. Leitzell, E. Lonnoy, J.B.R. Matthews, T.K. Maycock, T. Waterfield, O. Yelekçi, R. Yu, and B. Zhou (eds.)]. Cambridge University Press, Cambridge, United Kingdom and New York, NY, USA, pp. 817–922, https://doi:10.1017/9781009157896.008, 2021.

Taha, G., Loughman, R., Zhu, T., Thomason, L., Kar, J., Rieger, L., and Bourassa, A.: OMPS LP Version 2.0 multi-wavelength aerosol extinction coefficient retrieval algorithm, Atmos. Meas. Tech., 14, 1015–1036, https://doi.org/10.5194/amt-14-1015-2021, 2021.

Taylor, K. E., Crucifix, M., Braconnot, P., Hewitt, C. D., Doutriaux, C., Broccoli, A. J., Mitchell, J. F. B., and Webb, M. J.: Estimating Shortwave Radiative Forcing and Response in Climate Models, J. Climate, 20, 2530–2543, https://doi.org/10.1175/JCLI4143.1, 2007.

Thomason, L. W., Ernest, N., Millán, L., Rieger, L., Bourassa, A., Vernier, J.-P., Manney, G., Luo, B., Arfeuille, F., and Peter, T.: A global space-based stratospheric aerosol climatology: 1979–2016, Earth Syst. Sci. Dat., 10, 469–492, https://doi.org/10.5194/essd-10-469-2018, 2018.

Thornhill, G. D., Collins, W. J., Kramer, R. J., Olivié, D., Skeie, R. B., O'Connor, F. M., Abraham, N. L., Checa-Garcia, R., Bauer, S. E., Deushi, M., Emmons, L. K., Forster, P. M., Horowitz, L. W., Johnson, B., Keeble, J., Lamarque, J.-F., Michou, M., Mills, M. J., Mulcahy, J. P., Myhre, G., Nabat, P., Naik, V., Oshima, N., Schulz, M., Smith, C. J., Takemura, T., Tilmes, S., Wu, T., Zeng, G., and Zhang, J.: Effective radiative forcing from emissions of reactive gases and aerosols – a multi-model comparison, Atmos. Chem. Phys., 21, 853–874, https://doi.org/10.5194/acp-21-853-2021, 2021a.

Thornhill, G., Collins, W., Olivié, D., Skeie, R. B., Archibald, A., Bauer, S., Checa-Garcia, R., Fiedler, S., Folberth, G., Gjermundsen, A., Horowitz, L., Lamarque, J.-F., Michou, M., Mulcahy, J., Nabat, P., Naik, V., O'Connor, F. M., Paulot, F., Schulz, M., Scott, C. E., Séférian, R., Smith, C., Takemura, T., Tilmes, S., Tsigaridis, K., and Weber, J.: Climate-driven chemistry and aerosol feedbacks in CMIP6 Earth system models, Atmos. Chem. Phys., 21, 1105–1126, https://doi.org/10.5194/acp-21-1105-2021, 2021b.

Toohey, M. and Sigl, M.: Volcanic stratospheric sulfur injections and aerosol optical depth from 500\,BCE to 1900\,CE, Earth Syst. Sci. Data, 9, 809–831, https://doi.org/10.5194/essd-9-809-2017, 2017.

Trewin, B., Cazenave, A., Howell, S., Huss, M., Isensee, K., Palmer, M. D., Tarasova, O., and Vermeulen, A.: Headline Indicators for Global Climate Monitoring, Bulletin of the American Meteorological Society, 102, E20–E37, https://doi.org/10.1175/BAMS-D-19-0196.1, 2021.

Vose, R. S., Huang, B., Yin, X., Arndt, D., Easterling, D. R., Lawrimore, J. H., Menne, M. J., Sanchez-Lugo, A., and Zhang, H. M.: Implementing Full Spatial Coverage in NOAA's Global Temperature Analysis, Geophys. Res. Lett., 48, e2020GL090873, https://doi.org/10.1029/2020GL090873, 2021.

Watson-Parris, D., Christensen, M. W., Laurenson, A., Clewley, D., Gryspeerdt, E., and Stier, P.: Shipping regulations lead to large reduction in cloud perturbations, Proc. Natl. Acad. Sci. U.S.A., 119, e2206885119, https://doi.org/10.1073/pnas.2206885119, 2022.

Yuan, T., Song, H., Wood, R., Wang, C., Oreopoulos, L., Platnick, S. E., Von Hippel, S., Meyer, K., Light, S., and Wilcox, E.: Global reduction in ship-tracks from sulfur regulations for shipping fuel, Sci. Adv., 8, eabn7988, https://doi.org/10.1126/sciadv.abn7988, 2022.

Zelinka, M. D., Andrews, T., Forster, P. M., and Taylor, K. E.: Quantifying components of aerosol-cloud-radiation interactions in climate models, J. Geophys. Res.-Atmos., 119, 7599–7615, https://doi.org/10.1002/2014JD021710, 2014.

Zelinka, M. D., Smith, C. J., Qin, Y., and Taylor, K. E.: Aerosol Effective Radiative Forcings in CMIP Models, EGUsphere [preprint], https://doi.org/10.5194/egusphere-2023-689, 2023.